Research Paper

Correlation of pore size distribution with thermal conductivity of precipitated silica and experimental determination of the coupling effect

S. Sonnick[a,b,*], M. Meier[b], J. Ross-Jones[a,b], L. Erlbeck[a], I. Medina[a], H. Nirschl[b], M. Rädle[a]

[a] *Institute for Process Control and Innovative Energy Conversion, University of Applied Sciences Mannheim, Paul-Wittsack-Straße 10, 68163 Mannheim, Germany*
[b] *Institute for Mechanical Process Engineering and Mechanics, Karlsruhe Institute of Technology, Strasse am Forum 8, 76131 Karlsruhe, Germany*

HIGHLIGHTS

- Precipitated silica was tested for suitibility as core material for vacuum insulation.
- A guarded hot plate apparatus, measuring under vacuum conditions, was developed.
- Mercury intrusion porosimetry data were used to calculate gas-thermal conductivity.
- Model to predict thermal conductivity is presented (focus on coupling effect).

ARTICLE INFO

ABSTRACT

Vacuum insulation panels are high-performance insulating materials with considerably better thermal properties than conventional thermal insulation. Unfortunately, their use is limited to applications where their high price does not matter. To extend the application range of vacuum insulation, the authors try to replace the high-priced core material fumed silica with the cheaper precipitated silica. For this purpose, five commercially available precipitated silica samples were tested for their suitability as core material for vacuum insulations. They were pre-pressed with 5 bar and 30 bar each. To compare their thermal performances, a guarded hot plate apparatus for measuring thermal conductivities under vacuum was developed. The pore size distributions of the samples were measured by mercury intrusion porosimetry and used to calculate the gas thermal conductivity as a function of the residual pressure. For this purpose, a correction factor for the measured pore size distribution is introduced. Additionally, the coupling effect between gaseous and solid thermal conductivity could be determined through comparison with measured data. A model is presented to predict the thermal conductivity curve, even of unknown silica samples, solely using mercury intrusion porosimetry data.

1. Introduction

Thermal insulation materials are essential for sustainable energy management of processes and devices. Nowadays, most insulations consist of foam or fiber materials made of organic or inorganic base materials [1]. These conventional insulation materials all operate according to the same principle. They are composed of a wide network of solid material with air inclusions (pores) which are small enough to suppress convection within. The solid materials always have higher thermal conductivities than the included air. Thus the goal of manufacturers of conventional thermal insulation materials is to reduce the solid fraction as long as the conductivity of the insulation material approaches the value of air, which is $25.87 \frac{\text{mW}}{\text{mK}}$ at 20 °C [2]. Most conventional materials on the market reach thermal conductivities around 30–40 $\frac{mW}{mK}$.

Super-insulations operate on a principle based on the Knudsen effect, whereby the pore size of the material is of the same order of magnitude as or less than that of the mean free path of gas molecules. This leads to a phenomenon where the gaseous thermal conductivity inside the pores decreases. If the pore size is substantially smaller than the mean free path, thermal conductivity of the gas can be neglected. One possibility to achieve the Knudsen effect is to reduce the pore size. At atmospheric pressure, the pore size should be smaller than 65 nm at 20 °C so that it is smaller than the mean free path [3]. Alternatively, it is also possible to reduce the gaseous pressure inside the pores, which is the operating principle of vacuum insulation panels (VIP). Thus, super-insulations can reach lower overall thermal conductivity values as compared to free air. This special property makes such insulation

Nomenclature

Symbols

$\dot{Q}$	heat flux [W]
$\bar{x}$	average pore size [m]
D	fractal dimension [–]
d	diameter [m]
E	transport extinction coefficient [m^{-1}]
F	pressure load [bar]
f	coupling effect factor [–]
k_B	Boltzmann constant [J/K]
Kn	Knudsen number [–]
L	mean free path of molecules [m]
n	reflection index [–]
P	pressure of mercury intrusion porosimetry [Pa]
p	pressure [mbar]
T	temperature [K]
V	volume [m^3]
x	pore size [m]
Y	elastic modulus [Pa]
α	accommodation coefficient [–]
β	dimensionless coefficient for gaseous conductivity calculation [–]
γ	surface tension of mercury [Nm]
η	Poisson's ratio [–]
Θ	contact angle between mercury and silica [°]
κ	adiabatic coefficient [–]
λ	thermal conductivity [W/mK]
λ'	thermal conductivity of a single pore [W/mK]
$λ_0$	free gas thermal conductivity [W/mK]
σ	Stefan-Boltzmann constant [W/m^{2}K^4]
ϕ	porosity [m^3/m^3]

Subscripts and abbreviations

2d	two dimensional
3d	three dimensional
AM	air molecule
atm	atmospheric
c	coupling
g	gaseous
max	maximum/end of intrusion
r	radiative
s	solid
SM	solid material
sr	solid and radiative

materials very interesting for many applications where a good thermal dissociation is essential but space is limited, such as in cryogenic devices [4], heat storage tanks, in the building sector for restauration of historic monuments or if space inside the walls is required for thermal storage systems like phase change materials [5]. Most of the commercially available VIPs consist of core material mixtures made of fumed silica, because its nanoporous, hierarchical structure ensures low gaseous and solid conductivity values; some kind of opacifier to reduce radiation and fibers add mechanical stability to the material. The material is pressed, cut to the desired dimensions and sealed under vacuum in aluminized foils. These panels have thermal conductivities around 4–8 mW/mK right after production. Due to unavoidable minor leakages, the internal pressure increases constantly. The typical lifetime of a panel is estimated around 25 years [6], at which point the thermal conductivity doubles its initial value. For core materials made of fumed silica, this happens when the internal pressure reaches approximately 100 mbar. However, precipitated silica cores reach this point at around 10 mbar [6,7], while their initial value is basically the same. A great advantage of precipitated silica is its significantly lower price compared to fumed silica. Thus, precipitated silica can be attractive for some applications, such as thermal transport boxes, where long lifetimes are unnecessary. For this reason, the purpose of this work is to uncover correlations between thermal and structural properties, to understand the behavior of different precipitated silica samples for use in insulation materials, to ultimately define the perfect silica for the authors' application.

2. Measurements and analysis

To characterize and compare properties of different precipitated silica samples, five different types have been examined. The manufacturer of all samples is Grace Germany GmbH and the product names are Perkasil GT 3000 PD (GT), Syloid MX109 (MX), CP 513 – 11202 (CP), Perkasil KS 408 PD (KS) and Sylowhite SM 405 (SM). In the subsequent sections, the following shortcuts are used: GT, MX, CP, KS, SM. These are commercially available products and have been delivered in 15 kg or 25 kg bags. These samples were selected to get a good

overview of the company's product portfolio. All samples were prepared with external pressure loads of 5 bar and 30 bar with a hydraulic press. Furthermore, pore size distributions of all ten samples have been measured with mercury intrusion porosimetry and thermal conductivity over gas pressure, with a guarded hot plate apparatus.

2.1. Mercury intrusion porosimetry (MIP)

Mercury porosimetry analysis is the progressive intrusion of mercury into a porous structure under strictly controlled pressure [8]. Since the necessary pressure to intrude the non-wetting liquid mercury into a pore is inversely proportional to the pore size, it is possible to measure pore size distribution with this method. The main advantage is that it allows pore size analysis to be undertaken over a wide range of mesopore–macropore widths (routinely, from ca. 0.003 to ca. 400 µm) [9].

$$x(p) = -\frac{4\gamma cos(\Theta)}{P} \qquad (1)$$

MIP pore size distribution analysis is based on the Washburn equation (Eq. (1)) and on the assumption that pores are cylindrical and entirely and equally accessible to mercury. To calculate the minimum pore size *x* as a function of the particular mercury pressure level P, the surface tension of mercury γ and the contact angle between mercury and silica Θ are required. For the present work, $\Theta = 130\text{Â}°$, $\gamma = 0,485$ N/m and a "*AutoPore III (co. micromeritics, USA)*" were used.

Besides pore size distribution, MIP-data can be used to determine the surface fractal dimension *D* of the pores. In this case, the fractal dimension of a solid is a parameter characterizing the degree of roughness of its surface [8].

$$\log\left(\frac{dV}{dp}\right) = \log(C) + (D-4)\log(P) \qquad (2)$$

By double-logarithmic application of Eq. (2), where P is the mercury pressure, *V* is the volume of mercury intruded into the pores and C is a constant, the fractal dimension *D* of the pores can be determined from the slope.

2.2. Test apparatus for thermal conductivity at various pressure levels

To measure thermal conductivity of silica samples at various pressure levels, a test bench, which is able to operate under vacuum, has been developed. It operates according to the principle of a guarded hot plate apparatus [10], where the measuring area in the center of the apparatus is surrounded by guard heaters which avoid heat losses from the measuring area to the surroundings. The measuring principle is shown in Fig. 1.

The whole structure is placed in a vacuum chamber composed of a stainless steel tank. A view into the opened tank is shown on Fig. 2. With the rotary vane vacuum pump P1, the valve V1 and two pressure sensors P1.1 and P1.2 for different pressure levels, it is possible to regulate the internal pressure from approximately 0.05 mbar up to atmospheric pressure. Two samples of equivalent thickness, between 5 and 15 mm, are placed between the heating plate and the two cooling plates. When testing loose samples, the powder samples can be pressed directly into the mold within the chamber. Pressing directly into the mold avoids air gaps between the samples and the plates, which is one of the main advantages of this self-constructed apparatus compared to commercial devices. The mold, as well as the heating and cooling plates have a quadratic base area of $0.0256 \, \text{m}^2$. The primary heater H1, in the center of the heating plate, has a base area of $6.4 * 10^{-3} \, \text{m}^2$ and can be regulated to the requested heating plate temperature by electrical power. The guard ring H2 is regulated to the same temperature as H1 to ensure that all the heat from H1 flows towards the cooling plates and not into the surroundings. The cooling plates are made of aluminum and fit seamlessly into the mold. The plates contain spiraling channels with flowing cooling water to ensure an even temperature distribution. The temperature of the cooling water can be controlled by an external cryostat. In this way, the average temperature and range of interest can be chosen. Additionally, the outside temperature of the mold can be adjusted with heater H3 to isolate the chamber from the surrounding temperature. For all control loops, 12 PT100 temperature sensors T1.1 to T4.2 are positioned at several locations around the test stand.

Fig. 2. View into the opened vacuum chamber. Cooling plate 1 can be seen outside the sample mold. Both samples, the heating plate and the cooling plate 2 are already in position.

Table 1
Measurement uncertainty for components of the guarded hot plate apparatus.

Temperature measurements		
		Error
Thermocouple	PT100 (1/3 DIN)	± 0.18 K
Transducer	MU-PT100-I420	0.100%
NIDAQ	USB.6008	0.153%
	Total	**0.183%**
Power measurement		
		Error
Measure power	Shunt resistor	1.000%
NIDAQ	USB.6008	0.147%
	Total	**1.011%**
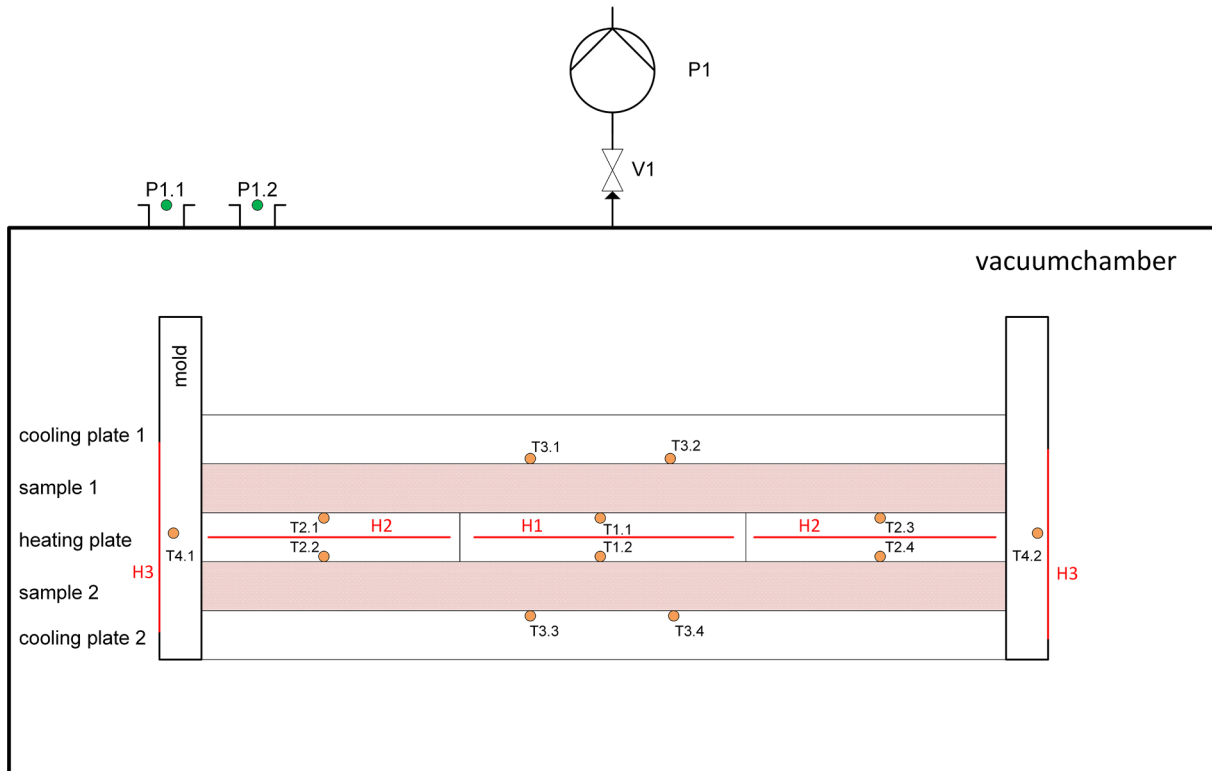
Fig. 1. Illustration of the test stand for measuring thermal conductivity at various pressure levels.

To characterize a sample, the chamber is evacuated to a pressure of approximately 0.05 mbar. After adjusting heating and cooling plate temperatures, it is necessary to wait until the temperature field is stable, which means the power input into H1 is constant. Power consumption of H1 as well as all temperature and pressure data are recorded every five seconds.

2.2.1. Uncertainty analysis of thermal conductivity measurement

Calculating the propagation of uncertainty using Table 1, together with the uncertainty for the thickness and area of the VIP, 1.5% and 1% respectively a total uncertainty of 2.07% for the thermal conductivity measurement is obtained.

To validate the device, a reference measurement needs to be performed. For this purpose a standard polystyrene board from NIST (National Institute of Standards and Technology) is used. At the present conditions (T = 30 °C and $\rho = 39.03 \frac{kg}{m^3}$) the test material is supposed to have a thermal conductivity of $0.0343 \frac{W}{mK} \mp 1.5\%$ [11]. The measured value of the newly developed guarded hot plate device is $0.0341 \frac{W}{mK}$. Thus, it matches perfectly within the uncertainty range of the test material.

Two capacitive pressure sensors are used, a "*MKS Baratron Type 122A*" and a "*Siemens SITRANS P200*" sensor to measure at low and high pressures respectively. Both sensors have a maximum uncertainty of 0.5%, whereas the "*MKS Baratron*" sensor is used between 0.01 and 14 mbar and the "Siemens" sensor between 14 mbar and atmospheric pressure.

3. Thermal transport theory and analytical model

Heat transfer in insulation materials is composed of three main mechanisms: solid thermal conductivity λ_s, radiative thermal conductivity λ_r (both mechanisms are only a function of temperature, which means for isothermal problems they can be assumed to be constant) and gaseous thermal conductivity λ_g which is a function of gas pressure p and the mean free path, for example the pore size x. A fourth mechanism which depends on the microscopic shape of the material and also on gas pressure is the coupling effect between solid and gaseous thermal conductivity λ_c [12]. λ_c is negligible for most foams [13] but plays a decisive role for silica based core materials, which are investigated in this work. Consequently, the thermal conductivity of an insulation material can be described as a sum of these four mechanisms as shown in Eq. (3) [13,14]. All heat transfer mechanisms are temperature dependent, however, in this work constant and steady state temperature are assumed.

$$\lambda(p) = \lambda_s + \lambda_r + \lambda_g(p) + \lambda_c(\lambda_g) \tag{3}$$

3.1. Solid thermal conductivity

Heat flow over the solid phase of a bulk powder λ_s depends on various material properties. Of course, the thermal conductivity λ_{SM} of the solid material itself plays an important role, but also the porosity ϕ and the thermal contact resistance between the particles are influential. The contact resistance is not easy to capture and depends on the Poisson's ratio η, the elastic modulus Y, the radius of the particles and the effecting pressure load F. These influences are summarized in Eq. (4), which is used by many authors to calculate solid thermal conductivity [4,15].

$$\lambda_s = 3,44(1-\phi)^{\frac{4}{3}}\left(\frac{1-\eta^2}{Y}\right)^{\frac{1}{3}}\lambda_{SM}F^{\frac{1}{3}} \tag{4}$$

3.2. Radiative thermal conductivity

In most macroscopic cases, radiation can be described with the Rossland approximation for optically thick materials. Thus, it is possible to calculate an equivalent conductivity λ_r using Eq. (5) [6].

$$\lambda_r = \frac{16\sigma n^2 T^3}{3E(T)} \tag{5}$$

In this case T is the radiative temperature and can be calculated with the surface temperatures of the sample T_1 and T_2 using Eq. (6), where $E(T)$ is the transport extinction coefficient, σ is the Stefan-Boltzmann constant and n the reflection index, $n \approx 1$ for opacified silica.

$$T = \sqrt[3]{\frac{(T_1^2 + T_2^2)(T_1 + T_2)}{4}} \tag{6}$$

To reduce radiative heat transfer, opacifiers such as carbon black, TiO_2 or silicon carbide are used. Caps and Fricke [16] found $E = 3600$ m^{-1} for pure precipitated silica and values up to $E = 26000$ m^{-1} for opacified precipitated silica.

3.3. Gaseous thermal conductivity

Considering the Knudsen effect, thermal conductivity of gases surrounded by a solid material is a function of geometric size and gas pressure or rather the mean free path of gas molecules. The Knudsen Number Kn is used to quantify the relation between the mean free path of molecules L and the geometric size of the confined space, for example the pore size x.

$$\lambda_g = \frac{\phi * \lambda_0(T)}{1 + 2 * \beta * Kn} \tag{7}$$

In Eq. (7) [4] λ_0 is the thermal conductivity of the gas at atmospheric pressure, ϕ is the porosity of the insulation material and β is a dimensionless coefficient depending on an accommodation coefficient α and the adiabatic coefficient of the gas κ. It can be calculated via Eq. (8) [4]. The accommodation coefficient is a measure for the quality of energy exchange between the gas molecules and the solid surface. The adiabatic coefficient is the relation between heat capacity at constant pressure c_p and heat capacity at constant volume c_v.

$$\beta = \frac{5\pi}{32} * \frac{9\kappa - 5}{\kappa + 1} * \frac{2 - \alpha}{\alpha} \tag{8}$$

The value for β for the relationship between air and nanoporous silica is taken from the following references and is assumed to be 1.5 for this paper: $\beta = 1.5$ [17], $\beta = 1.6$ [18], $\beta = 1.5$ [19]

3.4. Coupling effect

Using Eq. (3) it is assumed, that all thermal resistances are arranged in a simple parallel configuration. Basically this assumption is correct, but as already mentioned for most materials a coupling of the different heat transfer mechanisms occurs; for example a coupling between solid thermal conductivity and radiation [20] or, and this is the focus of the present study, a coupling between solid and gaseous thermal conductivity. If, at the microscopic scale, the heat resistance between two solid phases is lower by passing a gas phase than the solid path, the resulting thermal conductivity exceeds the expected sum of gaseous and solid thermal conductivity. The effect is mainly caused by intervening gas molecules in the contact area of two particles. Some models to describe the coupling between these two mechanisms have been proposed, in most of the cases for silica aerogels [21–23]. In the simplest case, the phenomenon can be described as a series connection of

thermal resistances. Swimm [24] describes, that for common insulation materials, where λ_s is significantly higher than λ_g the simple linear relation shown in Eq. (9) is valid.

$$\lambda_c = \lambda_g * f \tag{9}$$

In this model, all influencing parameters like the particle surface geometry near the area of particle to particle contact or the thermal conductivity of the solid are combined in one factor f. Heinemann [17] mentioned, that in a bed of glass spheres, comparing the total thermal conductivity of the evacuated and the non-evacuated specimen, the contribution from the gas is seven times as large as expected just from the thermal conductivity of still air. This would mean for a bed of glass spheres f would be 7.

3.5. Calculation of thermal conductivity of various silica samples via pore size distribution

To predict the thermal conductivity of the investigated precipitated silica samples, pore size distribution measured with MIP of the compacted powder have been used.

Calculation starts with the mean free path of the air molecules L as a function of gas pressure p [25].

$$L(p) = \frac{k_B * T}{\sqrt{2} * \pi * d_{AM}^2 * p} \tag{10}$$

With $k_B = 1.38 * 10^{-23}\frac{J}{K}$ as the Boltzmann constant, T for the absolute Temperature and $d_{AM} = 3.65 * 10^{-10}$ m as the mean diameter of air molecules.

Following, for every pore size x and gas pressure p the Knudsen number Kn can be calculated [4].

$$Kn(p, x) = \frac{L}{x} \tag{11}$$

This results in a matrix of Knudsen numbers, which can be used to determine the gaseous thermal conductivity for every pressure and pore size

$$\lambda'_g(p, x) = \frac{\lambda_0}{1 + 2 * \beta * Kn} \tag{12}$$

with λ_0 as the thermal conductivity of air at atmospheric pressure and β as a factor depending on interaction between the gas and the surface of the solid described in the section "gaseous thermal conductivity".

The overall gaseous thermal conductivity can now be calculated

$$\lambda_g(p) = \phi \int \lambda'_g \frac{dV}{V_{max}} dx \tag{13}$$

with V as the intrusion volume and V_{max} as the total intrusion volume measured with MIP.

As previously mentioned, the solid thermal conductivity λ_s and the radiative thermal conductivity λ_r can be assumed to be constant. Thus $\lambda_{sr} = \lambda_s + \lambda_r$ is an offset value, which can be determined by measuring thermal conductivity at a very low pressure level, where λ_g and λ_c are negligible.

4. Results and discussion

4.1. Results of thermal conductivity measurements

Each silica sample was measured twice with applied pressure loads of 5 bar and twice with 30 bar, over a range of 14 pressure levels between 0.05 mbar and atmospheric pressure. The results for all the samples are shown in Fig. 4 (dash and dash-dot lines). As expected, thermal conductivity approaches a constant value at very low internal pressures and increases between 1 mbar and 10 mbar. A characteristic behavior for nanoporous silica samples is a slope $\frac{d\lambda}{dp} > 0$ for $p_{atm} = 10^3$ mbar, which is evidence for the presence of pores smaller
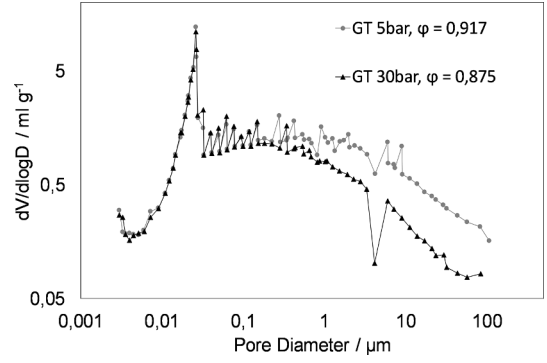
Fig. 3. Pore size distribution of "GT" prepared with two different pressure loads (5 bar and 30 bar), measured with mercury intrusion porosimetry, ϕ is the porosity of the sample.

than the mean free path of air molecules at atmospheric pressure (68 nm), following the Knudsen-theory.

4.2. Mercury intrusion porosimetry

To measure the pore size distribution of the investigated silica samples, each sample was prepared with different pressure loads (5 bar and 30 bar), heated at 350 °C and 50 mbar for 16 h and subsequently analyzed with mercury intrusion porosimetry. Fig. 3 shows the pore size distribution of the sample "GT" pressed with 5 bar and 30 bar respectively. It could be shown for all samples, that mechanical treating of the powder had negligible influence on pores smaller than about 200 nm. The measured pore size distribution can be used to calculate gaseous thermal conductivity, as it is necessary to know the volumetric percentage of every pore size.

4.3. Calculation of thermal conductivity without coupling effect

Thermal conductivity curve progressions calculated with $\lambda(p) = \lambda_{sr} + \lambda_g(p)$ and Eq. (10) are shown in Fig. 4 (solid and dotted lines), purposely leaving out the coupling effect. Therefore, λ_{sr} was taken from the measured value at the lowest gas pressure where no gaseous thermal conductivity is present. As expected, measured thermal conductivity rises faster than the calculated thermal conductivity due to the missing coupling effect. In all cases, the strongly compressed samples (30 bar) have a higher solid thermal conductivity than the less strongly compressed ones (5 bar) which leads to a higher offset in thermal conductivity. It can also be seen that the thermal conductivity of the 30 bar samples increases less strongly with an increase of the internal pressure than that of the 5 bar samples. This can be explained by the fact that the average pore size has decreased due to pressing. The average pore sizes of all samples (5 bar and 30 bar), related to the volumetric frequency are listed in Table 2.

The smaller pores lead to lower overall gaseous thermal conductivities at high gas pressure levels. In some cases (GT, KS and CP), this effect even causes an intersection of the 30 bar and 5 bar curves, although the solid conductivity and thus the starting point of the 30 bar curves are much higher.

On the other hand, taking a closer view at low pressure levels it is noticeable that the calculated curves rise faster than the experimental ones, although no coupling effect is considered, which leads to an intersection of both curves. In Fig. 4, this effect is only visible for GT - 5 bar (where the solid and the dashed lines intersect) but present for all samples. This may indicate that the measured pore sizes are too large. Most common uncertainties in terms of the mercury intrusion measurement, such as the bottle neck effect and compression of the sample, lead to an underestimation of the pore size [9,26,27]. Therefore, erroneous data of pore size distribution can be precluded as a reason for
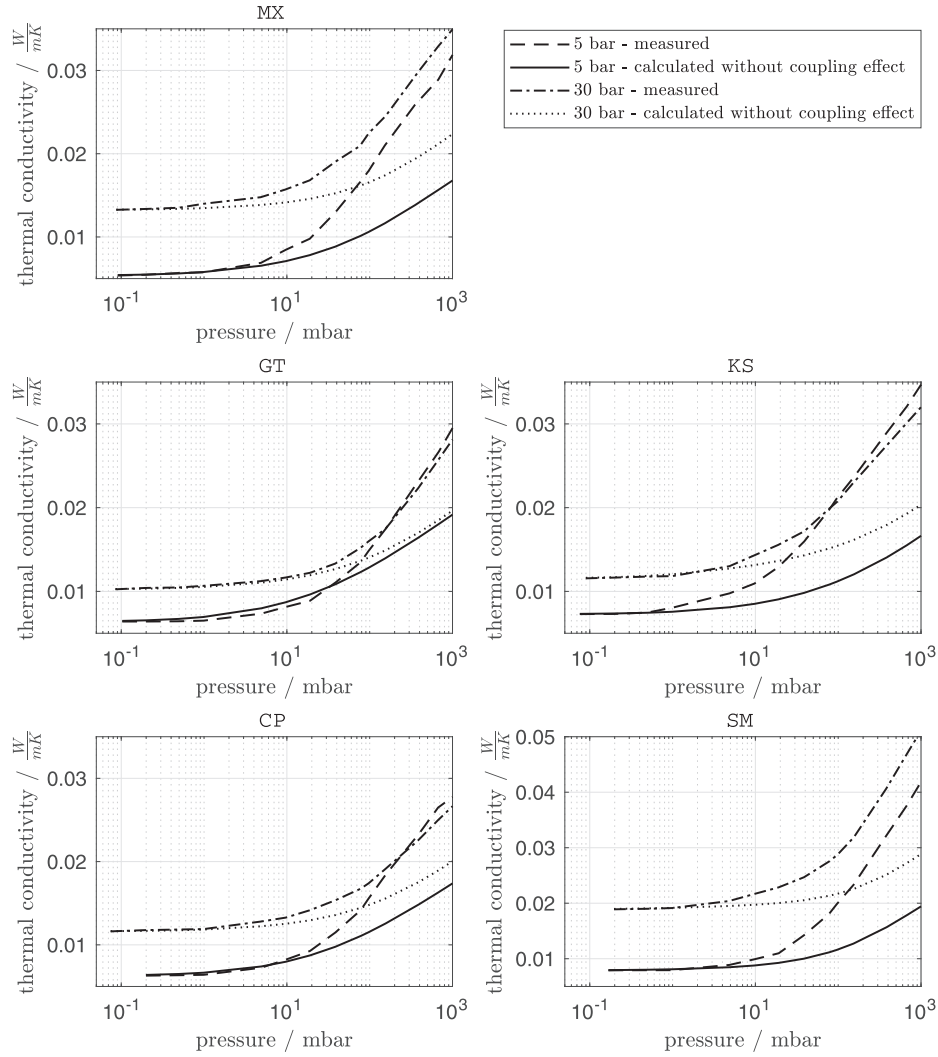
Fig. 4. Results of the thermal conductivity measurements of five samples of precipitated silica, pre-pressed with 5 and 30 bar compared to the corresponding calculated curves without consideration of the coupling effect.

Table 2
Average pore sizes of silica samples in μm.

Sample	MX	GT	KS	CP	SM
5 bar	6,0	6,7	3,7	4,4	2,8
30 bar	2,8	4,0	2,4	3,0	4,4

the present phenomenon. Just like most pore measuring methods, MIP in combination with the Washburn equation classifies pores by their internal pore width defined as the diameter of a cylindrical pore [28]. By using this pore size value for calculating the Knudsen number with Eq. (11) it is assumed, that the gas molecules inside the pores always "see" the largest possible distance between the pore walls. This assumption however is incorrect since gas molecules are evenly distributed throughout the whole system.

This means, the probability for a gas molecule to "see" in the direction of heat flow $\dot{Q}$, a smaller distance than the measured pore size is very high. The behavior is illustrated in Fig. 5. The average distance for a circular, two-dimensional pore can be calculated with the integral of the circular function of the unit circle.
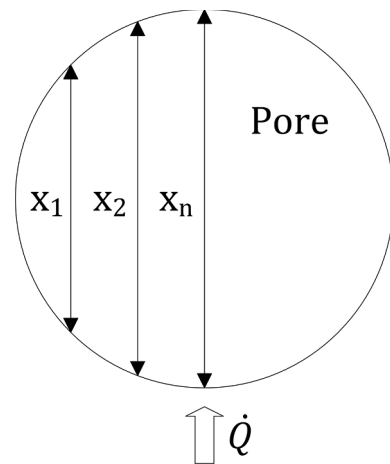
Fig. 5. Illustration of the available distances for a gas molecule inside a spherical pore.

$$\bar{x}_{2d} = \frac{1}{1-0} \int_0^1 \sqrt{1-x^2}\, dx = \frac{\arcsin(1)}{2} = \frac{\pi}{4} \tag{14}$$

Geometrically speaking, the result $\bar{x} = \frac{\pi}{4}$ is a quarter of the area of the unit circle. Extending this method to 3 dimensions, for a spherical pore, the mean distance equals one eighth of the unit sphere volume, which is $\frac{\pi}{6}$. Therefore, the following correction of the pore size distribution for spherical pores is assumed.

$$\bar{x} = \frac{\pi}{6} x \tag{15}$$

The correction leads to a curve with a smaller intersection-tendency and a better agreement with the measured values, especially in the low pressure range. Also for the following procedure of fitting the coupling effect factor, the correction of the pore size distribution data is helpful to obtain small deviations between the measured and calculated curves.

4.4. Determination of the coupling effect

The previous results visualize the important role of the coupling effect. For the present investigation the linear model from Swimm et al. [24] is used. It is determined that for most of the tested samples the model fits very well. Thus, the coupling effect factor f is determined by fitting the calculated curves to the experimental data using the method

Table 3

Coupling effect factor f, porosity ϕ measured with MIP and fractal dimension D for the five samples prepared with 5 bar and 30 bar external pressure load.

Sample		MX	GT	KS	CP	SM
5 bar pressure load	f	1.90	0.96	2.96	1.36	3.04
	ϕ	0.859	0.917	0.866	0.876	0.816
	D	3.15	3.04	3.18	3.11	3.12
30 bar pressure load	f	2.29	1.29	1.96	1.38	3.65
	ϕ	0.854	0.875	0.852	0.883	0.756
	D	3.19	3.17	3.04	3.25	2.89

of least squares. Therefore, in Eq. (9) only the parameter f is variable. The resulting curves, compared to the experimental results are shown in Fig. 6.

The obtained coupling effect factors f are listed in Table 3. Values from 0.96 for GT – 5 bar to 3.65 for SM – 30 bar are included. Also listed in Table 3 are the porosity ϕ and the surface fractal dimension D of the pore-surface, both determined by MIP.

The coupling effect basically depends on the relationship between gaseous and solid thermal conductivity, which is influenced by the geometry of the solid material. The basic structure of the five silica materials should be rather similar because they are all precipitated
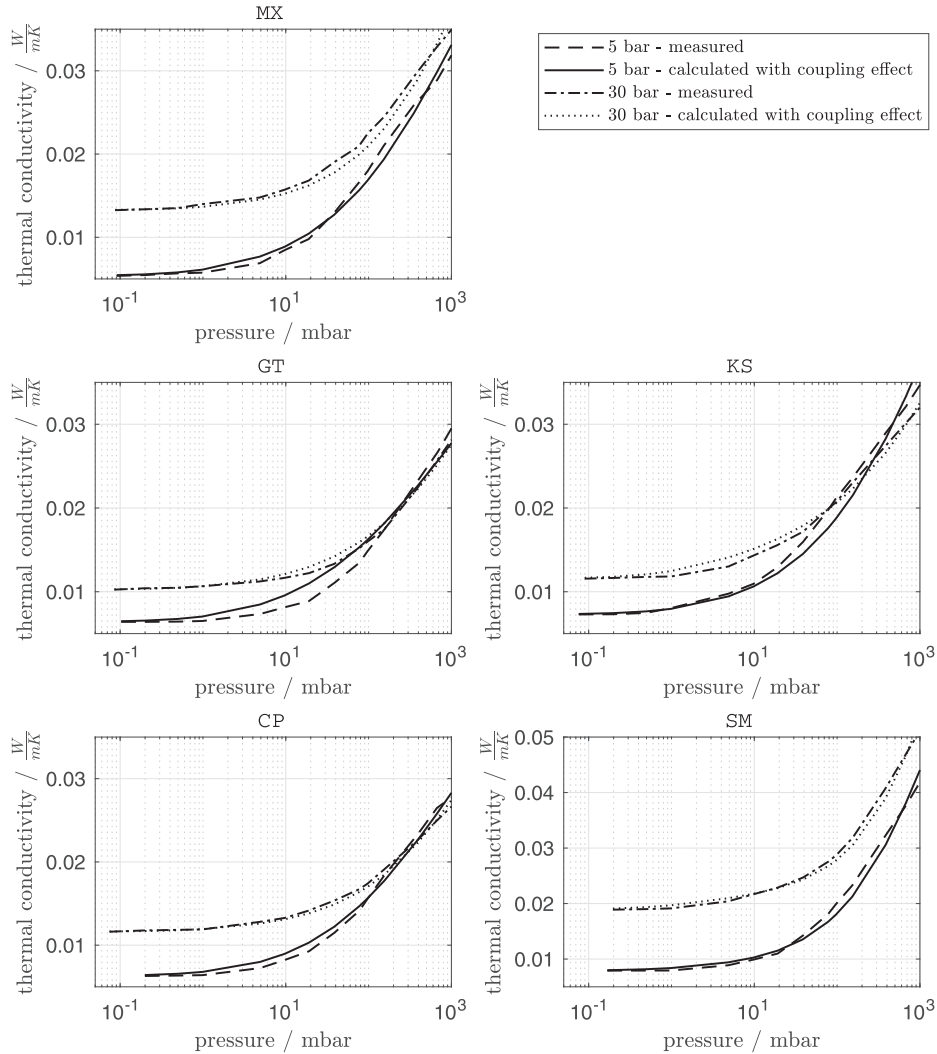
Fig. 6. Results of the thermal conductivity measurements of five samples of precipitated silica, pre-pressed with 5 and 30 bar compared to the corresponding calculated curves with adapted linear fitting parameter f.

silica, which means they consist of the same base material and are produced in similar processes. The similarity of the pore structure can be seen very clearly at the low fluctuations of the fractal dimension D in Table 3. According to the theory of fractal geometry, the fractal dimension of a surface must be in the range $2 < D < 3$. Nevertheless, it is not uncommon that fractal dimensions determined with MIP larger than 3 are obtained [29]. Therefore, the results can be used to compare the surface structures of the materials. In this regard, the values in Table 3 can all be classified as "very rough surfaces".

Moreover, with an increase in the bulk density of the pressed powder not only does the solid thermal conductivity increase, but also the number of spots where coupling between solid and gaseous conductivity can occur. Therefore, a linear relationship between the porosity ϕ and the coupling effect factor f was determined. For the investigated range of porosities $\phi = 0.76$ to $\phi = 0.92$ the corresponding linear function

$$f(\phi) = -18.68\phi + 17.94 \qquad (16)$$

is found. The coefficient of determination R^2 is 0.94, if one outlier (KS – 5 bar) is excluded, which is marked gray in Fig. 7. The function allows a good estimation of the coupling effect factor f, using data generated by mercury intrusion porosimetry only. Furthermore, gaseous thermal conductivity can be calculated using a measured pore size distribution in Eq. (13) and the coupling effect factor can be used to complete an adequate estimation of thermal conductivity as a function of gas pressure for any precipitated silica material.

5. Conclusion

The developed guarded hot plate apparatus delivers reliable results. The measured thermal conductivities of precipitated silica were as expected, but it also became clear that the simplified representations of precipitated silica as a core material for VIPs often presented in the literature were not applicable. In some cases, large differences between the products and the sample preparation had a considerable influence on the thermal properties. In the end, it was possible to develop a model to predict thermal conductivity as a function of gas pressure from available mercury intrusion porosimetry data. In particular, for the five investigated samples of precipitated silica, it is now possible to accurately predict the thermal conductivity as a function of gas pressure. Furthermore, extrapolations to predict the effect of alternative pore gases or the further thermal conductivity in higher pressure ranges are conceivable. Moreover, estimations for any unknown silica products or similar structures can be made with the new model. The estimation of the coupling effect as a function of porosity (Fig. 7) can help to make a preselection of new materials with regard to their suitability as thermal insulation, as manufacturers of precipitated silica often have the opportunity to measure pore size distributions by MIP. However, since precipitated silica is not very common for the application of thermal insulation yet, there is no information on thermal properties from the
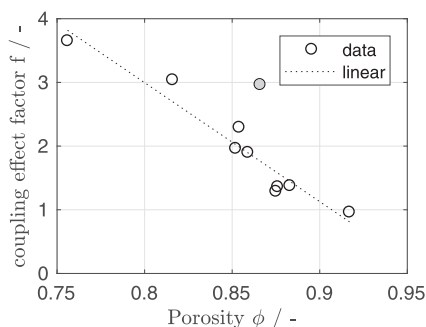
manufacturers. This gap can now be closed with the newly gained knowledge.

The comparison of the tested materials shows that the pore size distribution is a decisive influencing factor on the thermal properties of a silica product, nevertheless the coupling effect must not be neglected. Within the tested samples, the coupling effect is responsible for at least a doubling of the gaseous thermal conductivity for the material GT (5 bar) with f = 0.96 and can even cause a tremendous increase of λ_g with f = 3.65 (30 bar) for the material SM. The determined dependence of the coupling effect on the porosity ϕ leads to the realization that the optimization with regard to a low density of the silica based core material has a double relevance. A low density and thus high porosity leads, on the one hand, to a low solid thermal conductivity (Eq. (4)) and on the other hand to the mentioned low coupling effect. Thus, obviously pre-pressing the powders with high pressures does not lead to a decrease in the overall thermal conductivity of precipitated silica based core materials for vacuum insulation panels. In future work, attempts could be made to reduce the overall thermal conductivity by reducing the solid thermal conductivity. This should be possible by reducing the basic particle size and therefore increase the number of particle-particle resistances. Furthermore, investigating the effect of alternative pore gases could be helpful in order to validate the presented model and also as another strategy to decrease the overall thermal conductivity.

References

[1] A.M. Papadopoulos, State of the art in thermal insulation materials and aims for future developments, Energy Build. 37 (1) (2005) 77–86.
[2] V. e V, Ed., D2 Stoffwerte von bedeutenden reinen Fluiden, in: VDI-Wärmeatlas, Springer Berlin Heidelberg, 2013, pp. 175–356.
[3] S.G. Jennings, The mean free path in air, J. Aerosol Sci. 19 (2) (Apr. 1988) 159–166.
[4] M.G. Kaganer, Thermal insulation in cryogenic engineering, CERN Document Server, 1969. [Online]. Available: < http://cds.cern.ch/record/103864 > . (accessed: 08-Feb-2018).
[5] S. Sonnick, et al., Temperature stabilization using salt hydrate storage system to achieve thermal comfort in prefabricated wooden houses, Energy Build. 164 (2018) 48–60.
[6] M. Bouquerel, T. Duforestel, D. Baillis, G. Rusaouen, Heat transfer modeling in vacuum insulation panels containing nanoporous silicas—a review, Energy Build. 54 (2012) 320–336.
[7] J. Ross-Jones, M. Gaedtke, S. Sonnick, M. Rädle, H. Nirschl, M.J. Krause, Conjugate heat transfer through nano scale porous media to optimize vacuum insulation panels with lattice Boltzmann methods, Comput. Math. Appl., (2018).
[8] S. Lowell, J.E. Shields, M.A. Thomas, M. Thommes, Characterization of Porous Solids and Powders: Surface Area, Pore Size and Density, Springer, Netherlands, 2004.
[9] J. Rouquerol, et al., Liquid intrusion and alternative methods for the characterization of macroporous materials (IUPAC Technical Report), Pure Appl. Chem. 84 (1) (2011) 107–136.
[10] C16 Committee, Test Method for Steady-State Heat Flux Measurements and Thermal Transmission Properties by Means of the Guarded-Hot-Plate Apparatus, ASTM International.
[11] R.R. Zarr, A.L. Pintar, Standard reference materials: SRM 1453, Expanded Polystyrene Board, for Thermal Conductivity from 281 K to 313 K, Spec. Publ. NIST SP – 260-175, Dec. 2012.
[12] X. Lu, R. Caps, J. Fricke, C.T. Alviso, R.W. Pekala, Correlation between structure and thermal conductivity of organic aerogels, J. Non-Cryst. Solids 188 (3) (1995) 226–234.
[13] G. Reichenauer, U. Heinemann, H.-P. Ebert, Relationship between pore size and the gas pressure dependence of the gaseous thermal conductivity, Colloids Surf. Physicochem. Eng. Asp. 300 (1) (2007) 204–210.
[14] J. Fricke, U. Heinemann, H.P. Ebert, Vacuum insulation panels—From research to market, Vacuum 82 (7) (2008) 680–690.
[15] H. Reiss, K6 Superisolierungen, in: VDI-Wärmeatlas, V. e V, (Ed). Springer Berlin Heidelberg, 2013, pp. 1153–1220.
[16] R. Caps, J. Fricke, Thermal conductivity of opacified powder filler materials for vacuum insulations, Int. J. Thermophys. 21 (2) (2000) 445–452.
[17] U. Heinemann, Influence of water on the total heat transfer in 'evacuated' insulations, Int. J. Thermophys. 29 (2) (2008) 735–749.
[18] J. Fricke, H. Schwab, U. Heinemann, Vacuum insulation panels – exciting thermal properties and most challenging applications, Int. J. Thermophys. 27 (4) (2006) 1123–1139.
[19] R. Coquard, D. Quenard, Modeling of Heat Transfer in Nanoporous Silica - Influence of Moisture (2007), 13.
[20] R. Viskanta, R.J. Grosh, Heat transfer by simultaneous conduction and radiation in an

Fig. 7. Linear relationship of the porosity measured with MIP and the coupling effect factor f.

absorbing medium, J. Heat Transf. 84 (1) (1962) 63–72.

[21] C. Bi, G.H. Tang, Z.J. Hu, H.L. Yang, J.N. Li, Coupling model for heat transfer between solid and gas phases in aerogel and experimental investigation, Int. J. Heat Mass Transf. 79 (2014) 126–136.

[22] Z.-Y. Li, C.-Y. Zhu, X.-P. Zhao, A theoretical and numerical study on the gas-contributed thermal conductivity in aerogel, Int. J. Heat Mass Transf. 108 (2017) 1982–1990.

[23] J.-J. Zhao, Y.-Y. Duan, X.-D. Wang, B.-X. Wang, Effects of solid–gas coupling and pore and particle microstructures on the effective gaseous thermal conductivity in aerogels, J. Nanoparticle Res. 14 (8) (2012) 1024.

[24] K. Swimm, S. Vidi, G. Reichenauer, H.-P. Ebert, Coupling of gaseous and solid thermal conduction in porous solids, J. Non-Cryst. Solids 456 (2017) 114–124.

[25] S.Q. Zeng, A. Hunt, R. Greif, Mean free path and apparent thermal conductivity of a gas in a porous medium, J. Heat Transf. 117 (3) (1995) 758–761.

[26] J. Zhou, G. Ye, K. van Breugel, Characterization of pore structure in cement-based materials using pressurization–depressurization cycling mercury intrusion porosimetry (PDC-MIP), Cem. Concr. Res. 40 (7) (2010) 1120–1128.

[27] S. Diamond, Mercury porosimetry: an inappropriate method for the measurement of pore size distributions in cement-based materials, Cem. Concr. Res. 30 (10) (2000) 1517–1525.

[28] R.L. Carr, Evaluating flow properties of solids, 1965.

[29] B. Zhang, S. Li, Determination of the surface fractal dimension for porous media by mercury porosimetry, Ind. Eng. Chem. Res. 34 (4) (1995) 1383–1386.

Repository KITopen